Ceramics International 49 (2023) 34814–34825

Contents lists available at ScienceDirect

Ceramics International

journal homepage: www.elsevier.com/locate/ceramint

Multi-channel angular selective window based on the epsilon-near-zero features of $YaBa_2Cu_3O_7$ material and photonic crystals ceramic structure of extremely small dispersion edge regions

Bao-Fei Wan, Hai-Ning Ye, Hai-Feng Zhang *

College of Electronic and Optical Engineering & College of Flexible Electronics (Future Technology), Nanjing University of Posts and Telecommunications, Nanjing, 210023, China

ARTICLE INFO

Handling editor: P. Vincenzini

Keywords:
Multi-channel angular selective windows
Epsilon-near-zero properties
Superconductor
Multilayer ceramic photonic crystals

ABSTRACT

In this paper, the investigation of the angular selective windows (ASWs) is realized by constructing multilayer ceramic photonic crystals 1 (MCPC1) containing superconductor films $YaBa_2Cu_3O_7$ and air layers, MCPC2 composed of dielectrics layers of gallium arsenide ceramic (GaAs), silicon dioxide (SiO_2), and aluminium nitride ceramic (AIN), and MCPC3 made up of GaAs and SiO_2 films. The epsilon-near-zero (ENZ) properties of the superconductor in MCPC1 and the extremely small dispersion edge regions (DERs) in MCPC2 and MCPC3 provide criteria for angle selection. Organic combinations of three MCPCs can be used to achieve single-channel, dual-channel, three-channel, and four-channel ASWs. At the same time, the applicable working frequency bands for various channels are also studied. In particular, thanks to the lossless ENZ characteristics of $YaBa_2Cu_3O_7$, ultra-wideband single-channel ASWs of 220–1500 THz can be realized. In addition, the temperature change is also conducive to the control of ASWs position. As far as we know, there are few reports on the channel of ASWs at present, so we hope that the proposed design method will be beneficial to the research of improving the angular device.

1. Introduction

Frequency, polarization, and propagation direction are three basic properties of plane electromagnetic waves, and the researches on these three properties are critical [1–3]. Unlike the frequency system and polarization system, the development of the angle system has been very slow, which has been a huge challenge for scientists. However, the exploration of the angle system plays an important role in improving the investigation of electromagnetism and in practical applications, which is difficult to ignore. The ideal angle selection structure means that the electromagnetic wave can pass through completely in a certain angle range, and reflect completely in other angles [4–6]. This feature is suitable for reducing communication interference [7], suppressing the sidelobe signal of the antenna [8], improving solar energy absorption efficiency [9], optical communication [10], and privacy protection [11]. Therefore, scholars have put forward many positive design ideas for the exploration of perfect angle selection structure, such as Brewster angle [12], metamaterials [13], photonic crystals (PCs) [14], Fabry-Perot resonance [15], anisotropic metamaterials [16], near-zero refractive index metamaterials [17], etc. At present, the most extensive research and the most outstanding performance is the PCs structure.

PCs are a kind of artificial structure, which is formed by the periodic distribution of high and low refractive index medium. From the perspective of periodic distribution, PCs can be divided into one-dimensional PCs, two-dimensional PCs, and three-dimensional PCs [18–20]. Although the application of two-dimensional and three-dimensional structures has been gradually verified, one-dimensional PCs have been the most widely studied due to their simple structure and special optical characteristics. The two main features of PCs are photonic band gap and photonic energy localization, which provide new freedoms for controlling the propagation of electromagnetic waves [21–23]. Therefore, PCs show a strong charm in the fields of sensors, total reflectors, filters, absorbers, and logical computing. For angle selective structure, a large number of beneficial designs based on PCs have also been explored by predecessors. In 2014, Shen et al. [24] used the Brewster angle principle of PCs structure to

* Corresponding author. College of Electronic and Optical Engineering & College of Microelectronics, Nanjing University of Posts and Telecommunications, Nanjing, 210023, China.
E-mail address: hanlor@163.com (H.-F. Zhang).

https://doi.org/10.1016/j.ceramint.2023.08.155
Received 4 May 2023; Received in revised form 3 August 2023; Accepted 13 August 2023
Available online 19 August 2023

propose a small angular selective window (ASW) for the TM wave, which is not realized for the TE one. In 2018, Tanaka et al. [25] utilized the extremely small wave vector region of PCs structure to achieve a large ASW independent of polarization, but its working bandwidth was narrow. In 2018, Qu et al. [26] introduced a half-wave plate device on the basis of the Brewster angle structure to realize wide-band ASWs and overcome the polarization dependence problem. However, the bounding characteristics of the edge still need to be improved. In 2023, Wan et al. [27] realized an ASW with strong selection characteristics based on epsilon-near-zero (ENZ) characteristics of single negative media and explored the sensing characteristics of ENZ edges, which has provided a new idea for the development of angular structures. It can be observed that predecessors have made a lot of expansion on the development of ASWs based on PCs, focusing on polarization, bandwidth, scale, and other aspects. Nevertheless, in some special applications, such as antenna radiation, privacy protection, and other systems, the number of channels in the ASWs is also very important, although this aspect is rarely reported.

In this paper, to make up for the shortcomings of traditional research on multi-channel ASWs, the controllable channels are proposed by designing multiple multilayer ceramic photonic crystals (MCPCs) structures. The $YaBa_2Cu_3O_7$ layers are introduced into MCPC1 to achieve the angular edge of the ENZ property. The dielectrics of gallium arsenide ceramic (GaAs), silicon dioxide (SiO_2), and aluminium nitride ceramic (AIN) are designed as thin film structures to achieve MCPC2 and MCPC3, and to excite minimal dispersion edge regions (DERs) to achieve corresponding angular edges. MCPC1 is conducive to the realization of single-channel ASWs, the combination of MCPC1 and MCPC2 realizes the two-channel ASWs, the cascade of MCPC2 and MCPC3 induces three channels, and under the combined action of MCPC1, MCPC2, and MCPC3, the four-channel ASWs will occur. In addition, the bandwidth characteristics and temperature effects of ASWs for different channels are also discussed.

2. Structure design and investigation

In Fig. 1, the propagation direction of wave vector k is in the yoz plane, while the electric field direction of the TE wave is perpendicular to the plane of the propagation direction, and the magnetic field direction of the TM wave is perpendicular to the propagation plane. In order to realize multi-channel ASW, three MCPCs structures are designed. Each MCPCs structure consists of a host structure responsible for angle selection and anti-reflection structures for suppressing electromagnetic wave leakage in the window. For MCPC1, in the host structure, the thickness of $YaBa_2Cu_3O_7$ layer is 2000 nm. In the anti-reflection structures, the thicknesses of $YaBa_2Cu_3O_7$ layers and air layers are 65 nm and 40 nm, respectively. For MCPC2, in the host structure, the thicknesses of SiO_2 layers and GaAs layers are 250 nm and 352 nm, respectively. In the anti-reflection structures, the thicknesses of SiO_2 layers and AIN layers are 225 nm and 15 nm. However, for MCPC3, in the host structure, the thicknesses of GaAs layers and SiO_2 layers are 597 nm and 547 nm. To improve the transmittance of the ASWs, in the anti-reflection structures, for the TE wave, the thicknesses of SiO_2 layers and GaAs layers are 107 nm and 403 nm. For the TM wave, the thicknesses of SiO_2 layers and GaAs layers are 115 nm and 405 nm.

For $YaBa_2Cu_3O_7$ materials, the dielectric function is described by the two-fluid model and London local electrodynamics. When the temperature is lower than the critical temperature, the superconductor can be

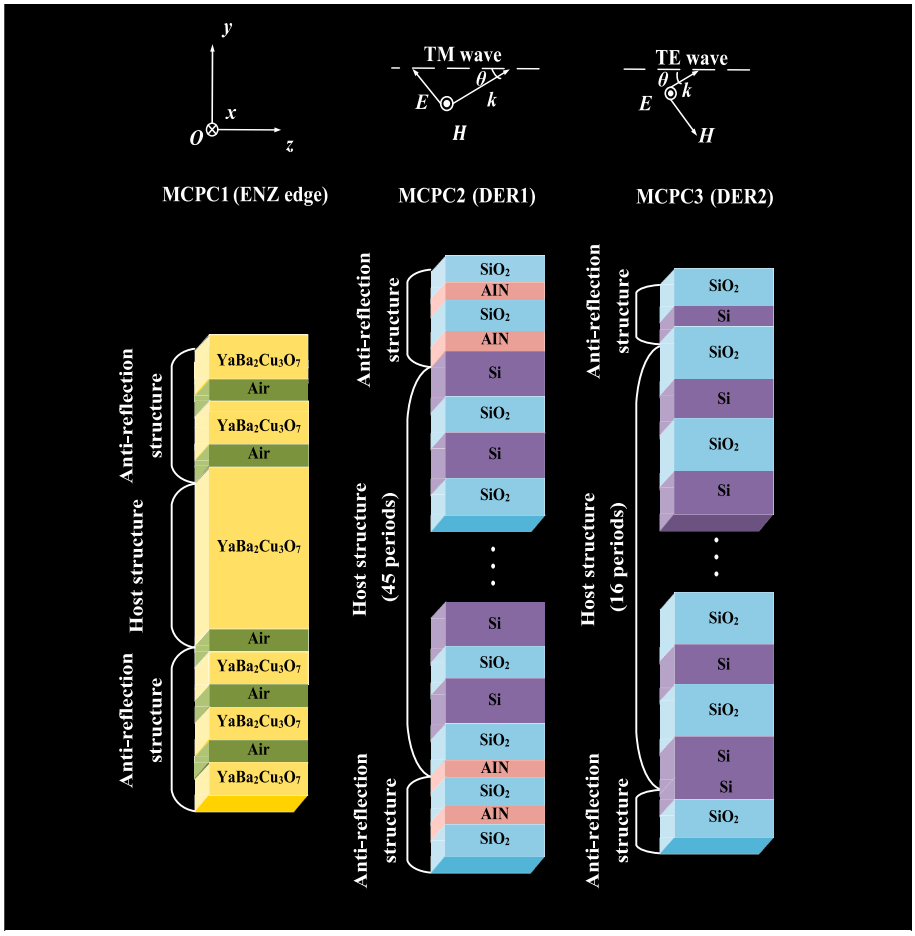

Fig. 1. The proposed angle selection structure diagram. The incident wave propagates in the direction of $+z$ the angle between the wave vector k and the $+z$ axis is θ.

regarded as lossless, and the dielectric function model can be described as [28]:

$$\varepsilon_Y = 1 - \frac{1}{\omega^2 \mu_0 \varepsilon_0 \lambda_L^2} \tag{1}$$

where, λ_L is the temperature-dependent London penetration length which is given by [28],

$$\lambda_L = \frac{\lambda_L(o)}{\sqrt{1 - \left(\frac{T_0}{T_C}\right)^P}} \tag{2}$$

$\lambda_L(o)$ is the London penetration length at $T_0 = 0$ K, $P = 4$, and $T_C = 92$ K is the superconducting critical temperature.

The refractive indices of SiO_2, GaAs, and AlN are 1.45, 3.45, and 2.15, respectively. In the case of the ultra-low temperature, the effects of the thermal expansion coefficients and thermo-optic coefficients are also considered [28],

$$d^* = d + ad\Delta T \tag{3}$$

$$n^* = n + bn\Delta T \tag{4}$$

In which, d and n are the thickness and refractive index at room temperature, and d^* and n^* are the thickness and refractive index at ultra-low temperature. α is the thermal expansion coefficient of the medium. For SiO_2, GaAs, and AlN, the values of a are $a_1 = 6.8 \times 10^{-6}/^oC$, $a_2 = 2.5 \times 10^{-4}/^oC$, and $a_3 = 6 \times 10^{-5}/^oC$. b is the thermo-optic coefficient of the medium. For SiO_2, GaAs, AlN and $YaBa_2Cu_3O_7$, the values of b are $b_1 = 2.6 \times 10^{-6}/^oC$, $b_2 = 5.73 \times 10^{-6}/^oC$, $b_3 = 4.5 \times 10^{-6}/^oC$ and $b_4 = 2 \times 10^{-5}/^oC$. In the absence of special instructions, the operating temperature T_0 is 55 K, and ΔT refers to the difference from room temperature.

The connection between different media layers is achieved through the transfer matrix method as follows [27],

$$M = \begin{bmatrix} M_{11} & M_{12} \\ M_{21} & M_{22} \end{bmatrix} \tag{5}$$

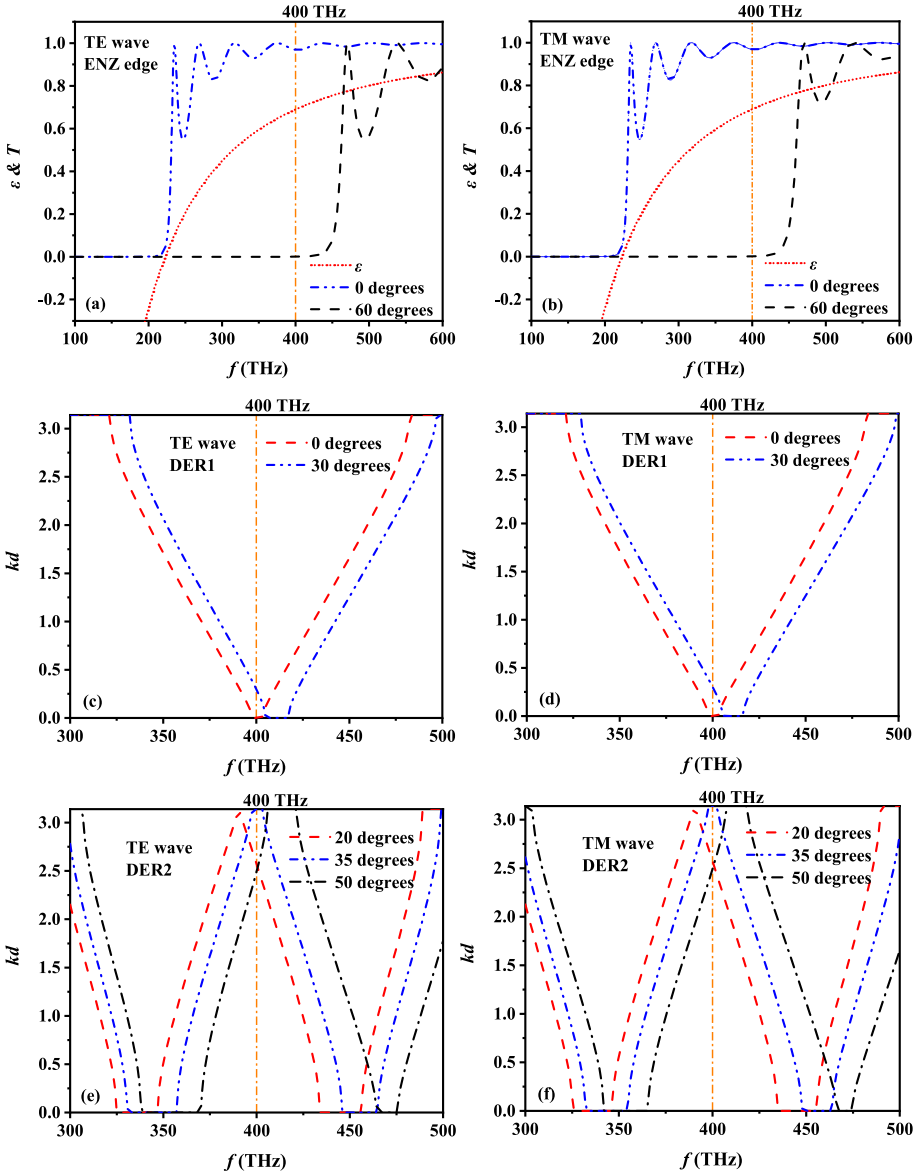

Fig. 2. The variation trend of dielectric constant of $YaBa_2Cu_3O_7$ medium and the transmissivity of the ENZ edge under (a) the TE wave, and (b) the TM wave. The dispersion distribution of DER1 affected by the angle regulation under (c) the TE wave, and (d) the TM wave. The dispersion distribution of DER2 influenced by the angle regulation under (e) the TE wave, and (f) the TM wave.

The film matrix of each layer can be determined by the following forms,

$$M_i = \begin{bmatrix} \cos\delta_i & -jp_i^{-1}\sin\delta_i \\ -jp_i\sin\delta_i & \cos\delta_i \end{bmatrix} \quad (6)$$

Among them, $\delta_i = (2\pi/\lambda)n_i d_i \cos\theta_i$, where $\lambda = 2\pi c/\omega$, $c = 3\times10^8$ m/s, $p_{i=}\sqrt{\varepsilon_0/\mu_0}n_i\cos\theta_i$ (TE wave), or $p_{i=}\sqrt{\varepsilon_0/\mu_0}n_i/\cos\theta_i$ (TM wave) [27]. μ_0 is the permeability of vacuum. $f = 400$ THz indicates the frequency.

The transmission coefficient t can be described by the following formulas:

$$t = \left|\frac{2p_0}{(M_{11}+M_{12}p_0)p_0 + (M_{21}+M_{22}p_0)}\right| \quad (7)$$

As a result, transmittance T is presented as:

$$T = |t|^2 \quad (8)$$

3. Analysis and discussion

3.1. Principle interpretation

To enhance the visualization effect, the frequency point of 400 THz is selected for investigation. In Fig. 2(a), when the incident angle is 0° if the dielectric constant of $YaBa_2Cu_3O_7$ material is converted from the negative value to the positive value, the corresponding electromagnetic wave energy will also be induced from strong reflection to high transmission, and the jump characteristic is obvious. It is noteworthy that the conversion node of electromagnetic wave energy coincides with the ENZ node of the dielectric constant. With the increase of the incident angle, the transmission area will produce a blueshift phenomenon. In the process of increasing the incident angle from 0° to 60°, the transmission area will move from the left side of 400 THz to the right side, which also means that if the incident frequency is 400 THz, the transition from transmission to reflection will occur, forming a specific ASW. In Fig. 2 (b), similar phenomena also occur, which means that the formation of ASW is independent of polarization. In Fig. 2(c), for the TE wave, when the incident angle is 0°, the frequency of 400 THz falls on the DER1, and kd is 0, which means that the region belongs to the forbidden band and the electromagnetic wave is completely reflected. As the incident direction tilts and the angle increases to 30°, DER1 moves toward the high-frequency direction and leaves 400 THz. At this time, the frequency point presents a transmission state. Therefore, the corresponding ASW will also be formed in the range of 0–30°. In Fig. 2(d), the incident TM wave will also cause DER1 to generate a simulated moving track and excite ASW in the range of 0–30°, which shows that the angle selection characteristic of DER1 is also polarization independent. In Fig. 2(e) and (f), the region of $kd = \pi$ is the photonic band gap at an incident angle of 20°, implying that DER2 falls completely to the left of the frequency point and that electromagnetic wave is able to traverse the structure. At an incident angle of 35°, DER2 generates a blueshift that covers 400 THz, preventing energy propagation. As the angle continues to tilt to 50°, DER2 again moves away from the analyzed frequency point, and the transmission phenomenon reappears. By analyzing the whole movement process, it can be seen that a very small angle band gap will be created between 20° and 50°, and at 35°, the energy valley will be generated.

In order to show the formation principle of multichannel ASW more clearly, the transmission curves of structures MCPC1 (ENZ edge), MCPC2 (DER1), and MCPC3 (DER2) in the angle domain are given in Fig. 3. In Fig. 3(a), in the case of TE wave incidence, for the ENZ edge, a transmission window is formed in the range of −54.8°–54.8°, while a high reflection phenomenon is formed in other angle regions. For DER1, a reflection window is formed in the range −17.8°–17.8, but transmission occurs in other regions. For DER2, reflection windows are generated at −41.6° ∼ −30° and 30°–41.6°, and energy from other angles is transmitted. In general, the number of ASW channels can be controlled by inserting different reflection windows into the transmission window. In Fig. 3(b), a similar phenomenon occurs for the TM wave.

3.2. Single-channel ASWs in MCPC1

Under the sole action of the ENZ edge, a wide single-channel ASW will be excited. In Fig. 4, a similar ASW occurs regardless of the polarized wave, and the bandwidth spans the range of 220–1500 THz. As the frequency rises, the angle of coverage rapidly spreads from 0°, and the speed of angle expansion gradually slows and eventually tends to stabilize around 80°. After analysis, two main reasons for the wide frequency bandwidth can be obtained. On the one hand, the calculation of dielectric constant of superconducting materials is similar to the Drude model, such as the InSb model, and plasma model. However, due to the existence of London penetration length, the permittivity of a superconductor is several orders of magnitude less sensitive to frequency change than that of other media. Therefore, even if the incident frequency changes greatly, the adjustment of permittivity is weak and always stays within the range of impedance matching. On the other hand, in the anti-reflection structures, the superconductor material layer is also introduced, so that when the external conditions change, the impedance of the anti-reflection structures will change simultaneously with the host structure, forming a dynamic impedance matching effect, thus enhancing the frequency bandwidth.

For the sake of enhancing the visualization effect, the angle distribution at an incident frequency of 400 THz is selected for a detailed explanation. In Fig. 5(a), for the TE wave, the ASW ranges from −54.8° to 54.8°. In the whole range, the transmittance exceeds 0.9, and the edges show excellent selectivity. In Fig. 5(b), if the polarization form is the TM wave, the covered angle range will become −54.9°–54.9°, in the case that the transmittance is still maintained above 0.9, and the edge selectivity is also maintained at a high level. In order to visually observe the edge selection characteristics of ASWs, the polar coordinates maps in Fig. 5(c) and (d) are also depicted. It can be seen that the single-channel

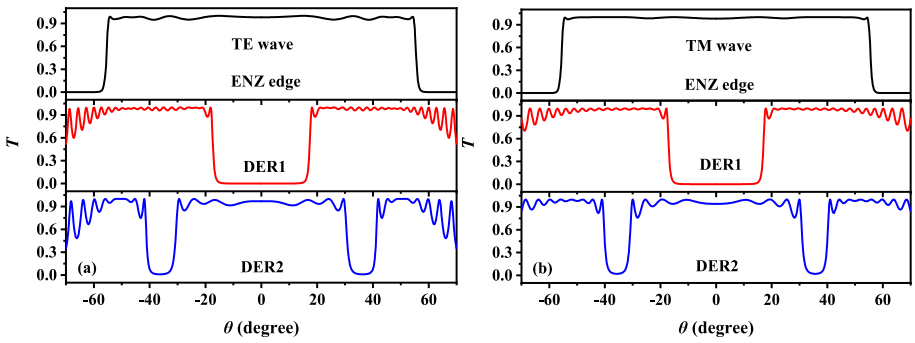

Fig. 3. Angle selectivity of three layered structures with $f = 400$ THz, (a) TE wave, (b) TM wave.

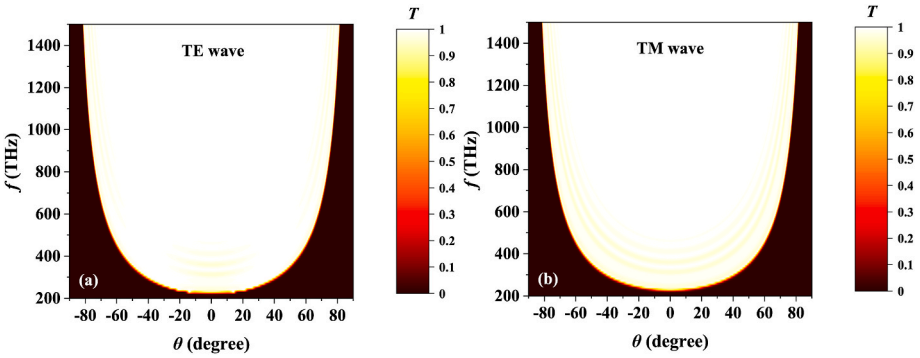

Fig. 4. The modulation of the single-channel ASWs by the adjustment of the incident frequency under (a) the TE wave and (b) the TM wave.

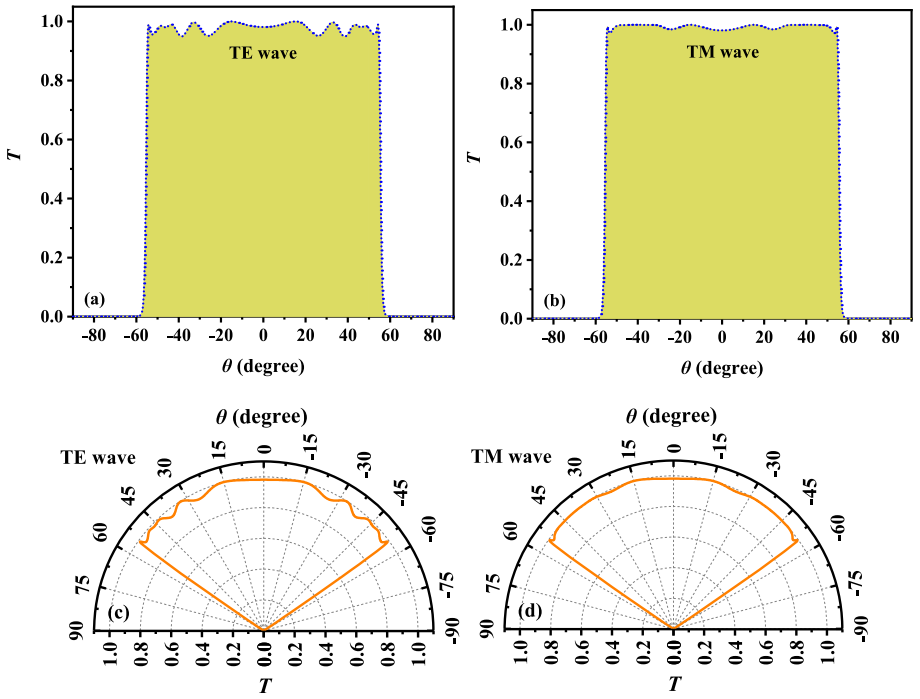

Fig. 5. The single-channel ASWs of 400 THz under the action of the ENZ edge under (a) the TE wave and (b) the TM wave. Direction selection diagrams of (c) the TE wave incidence and (d) the TM wave incidence.

ASWs are neither dependent on polarization nor produce polarization separation phenomenon. This is due to the fact that the generation of ASWs mainly depends on the ENZ property, and this dielectric constant property belongs to the physical property of the superconductor itself, which is not affected by the polarization form. The proposed feature can be described as pattern-free, which plays an important role in optical privacy protection, solar energy acquisition, and other fields.

Since the dielectric property of $YaBa_2Cu_3O_7$ is regulated by temperature, the influences of T_0 on ASWs are explored in Fig. 6. In Fig. 6(a), under the threshold of critical temperature, when T_0 extends from 10 K

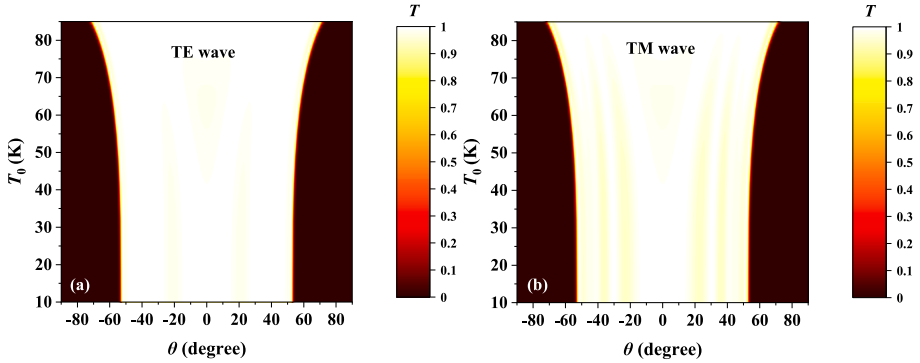

Fig. 6. The regulation of T_0 on the single-channel ASWs for (a) the TE wave and (b) the TM wave.

to 85 K, the excitation of the TE wave will force the range of ASWs to increase from −52.2–52.2° to −70.2–70.2°. In the relatively low-temperature range, the change of ASWs is not obvious when T_0 is below 40 K. As the temperature continues to rise, the trend of angle range enlargement will be obvious until the extension of −70.3–70.3°. By virtue of pattern-free characteristics, a similar phenomenon can be generated for the TM wave incidence in Fig. 6(b). If the temperature continues to increase from 10 K to 85 K, the range of ASWs involved will change from −52–52° to −70.2–70.2°, and the trend of angle adjustment is still slow first and then fast.

3.3. Two-channel ASWs under the cascade of MCPC1 and MCPC2

If the ENZ edge is combined with the DER1 region, two-channel ASWs will be generated. In Fig. 7(a), for the TE wave, the dual-channel phenomenon is maintained within the bandwidth of 398–404 THz. With the increase of frequency, the ranges of ASWs are reduced, and the outer edge approximation does not change, while the inner edge moves in the direction of a large angle. If the incident frequency is 398 THz, the angle range is −54.6 ~ −9° and 9–54.6°, and if the frequency becomes 404 THz, the corresponding value is −55.2 ~ −28.8° and 28.8–55.2°. In Fig. 7(b), for the TM wave, the phenomenon of double-channel ASW is also approximately maintained within the range of 398–404 THz. In the process of frequency drift, the maximum ranges covered by ASW are −54.5 ~ −8.9° and 8.9–54.5°, and the minimum ranges are −55.5 ~ −28° and 28–55.5°. The maximum range is obtained at 398 THz and the minimum range is obtained at 404 THz. Therefore, the increase in frequency also forces the reduction of the angle range. The analysis shows that the two edges of the outermost channel are determined by the ENZ edge, while the inner two edges are controlled by DER1, which is more susceptible to frequency. In addition, pattern-free characteristics are also significant, which is of great significance for the new type of optical anti-counterfeiting.

In Fig. 8(a), two channels with a symmetrical arrangement are generated under the excitation of the TE wave with a frequency of 400 THz. The ranges of channels are −54.8 ~ −17.8° and 17.8–54.8°. The overall transmittance is higher than 0.85, and the edge selectivity is obvious. In Fig. 8(b), supposing that the TM wave is incident, the range of the two channels are −55.3 ~ −17.5° and 17.5–55.3°, which still presents a symmetrical arrangement, and the transmissivity and edge selectivity distribution are also maintained at a high level. Under different polarization waves, the ranges of ASWs are not very different, which can be basically considered pattern-free. It is clear that the outsides of both channels are controlled by the ENZ edge and are therefore unaffected by polarization. The inner edges are controlled by DER1, the polarization separation phenomenon is generally obvious at a large angle, while a pattern-free phenomenon will be generated at a small angle. The polar coordinates maps in Fig. 8(c) and (d) are also depicted to visually observe the edge selection characteristics of ASWs. Significantly, the four edges of the ASWs show excellent selectivity throughout the interval.

In Fig. 9(a), for the TE wave incidence, with the increase of T_0, the angle range presents a trend of first shrinking and then expanding, and moving in the direction of a large angle. When T_0 is 35 K, the region covered by ASWs are −52.5 ~ −9.4° and 9.4–52.5°, and when T_0 rises to 85 K, the corresponding angles are −67.8~ −26.6° and 26.6–67.8°. In Fig. 9(b), the increase in T_0 also causes the ASWs excited by the TM wave to experience similar effects to the TE wave. The ASWs ranges at 35 K are −53 ~ −9.3° and 9.3–53°, and the ASWs ranges at 85 K are −68.4 ~ −25.6° and 25.6–68.4°. The main reason for the angle shift is that the enhancement in temperature increases the refractive index of superconductors and other materials, thus changing the optical path of electromagnetic wave propagation in the structure and affecting the ASWs.

3.4. Three-channel ASWs under the cascade of MCPC2 and MCPC3

In Fig. 10, both the TE and TM waves produce the three-channel ASWs under the action of the ENZ edge and DER2. The middle channel is wide and the channels on both sides are relatively narrow. For the TE wave in Fig. 9(a), with the increase in frequency, the range of the middle window gradually expands, while the window on both sides gradually shrinks. When the frequency is 395 THz, the ASWs are −53.7 ~ −33.1°, −24.2–24.2°, and 33.1–53.7°. If the frequency goes up to 407 THz, the three channels are in the range of −55.9 ~ −53.1°, −37.3–37.3°, and 53.1–55.9°. In Fig. 10(b), in the case of the TM wave incidence, the increase in frequency also leads to the expansion of the middle window and the narrowing of a window on both sides. When the frequency is 395 THz, the ASWs are −54.3 ~ −32.4°, −24.2–24.2°, and 32.4–54.3°. If the frequency rises to 410 THz, the three channels are −56.6 ~ −55.1°, −40.9–40.9°, and 53.1–55.9°.

In Fig. 11(a), for the TE wave, the ASWs ranges are −55 ~ -41.6°, −30–30°, and 41.6–55°. In the whole range, the transmittance exceeds 0.78, and the edges show good selectivity. In Fig. 11(b), if the polarization form is the TM wave, the angle ranges covered will become −55 ~ -40.7°, −30.4–30.4°, and 40.7–55°, the transmittance is still maintained above 0.75, and the edge selectivity is also maintained at a high level. The polar coordinates maps in Fig. 11(c) and (d) are also depicted to visually observe the edge selectivity of ASWs.

In Fig. 12(a), for the TE wave, when T_0 is 10 K, the regions covered by ASWs are −51.5 ~ −34.3°, −26.6–26.6°, and 46.6–68.9°, and when T_0 rises to 85 K, the corresponding angles are −68.9 ~ −46.6°, −32.2–32.2°, and 34.3–51.5°. In Fig. 12(b), the ASWs ranges at 10 K are −52.4 ~ −33.7°, −26.9–26.9°, and 33.7–52.4°, and the ASWs ranges at 85 K are −68.1 ~ −45°, −32.7–32.7°, and 45–68.1°. The middle window scope increases only slightly, while the sides of the window shift significantly in the direction of large angles.

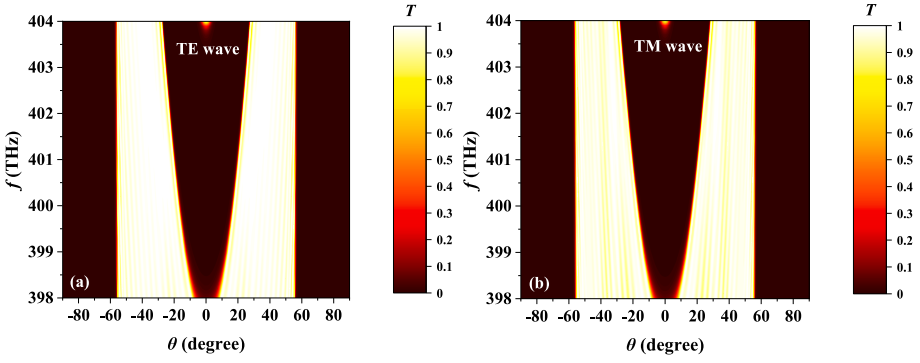

Fig. 7. The modulation of the dual-channel ASWs by the adjustment of the incident frequency under (a) the TE wave and (b) the TM wave.

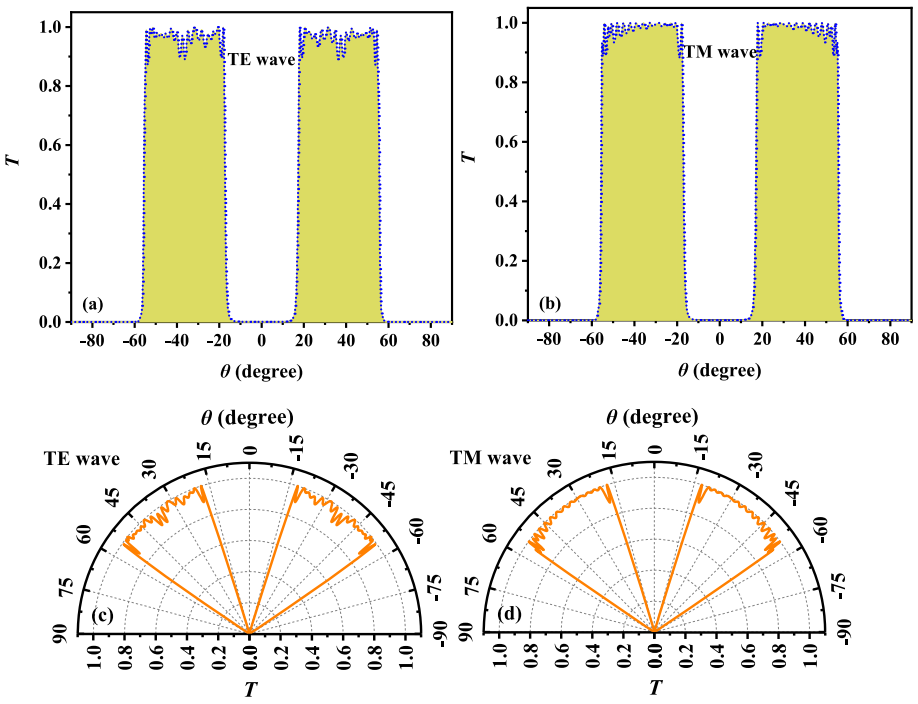

Fig. 8. The dual-channel ASWs of 400 THz under the action of the ENZ edge and DER1 under (a) the TE wave and (b) the TM wave. Direction selection diagrams of (c) the TE wave incidence and (d) the TM wave incidence.

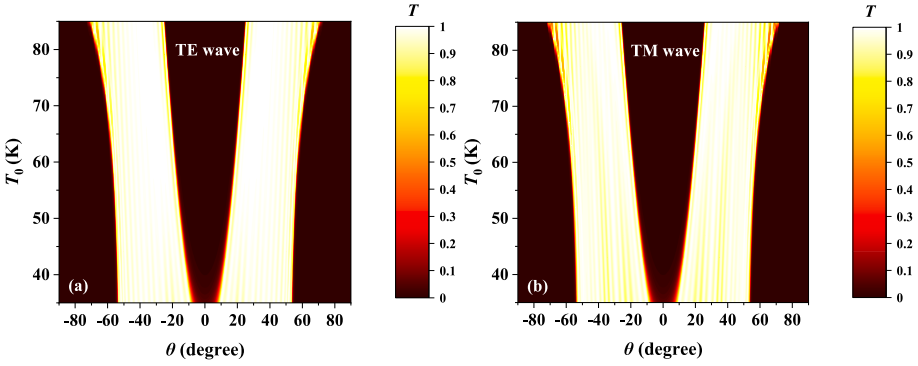

Fig. 9. The regulation of T_0 on the dual-channel ASWs for (a) the TE wave and (b) the TM wave.

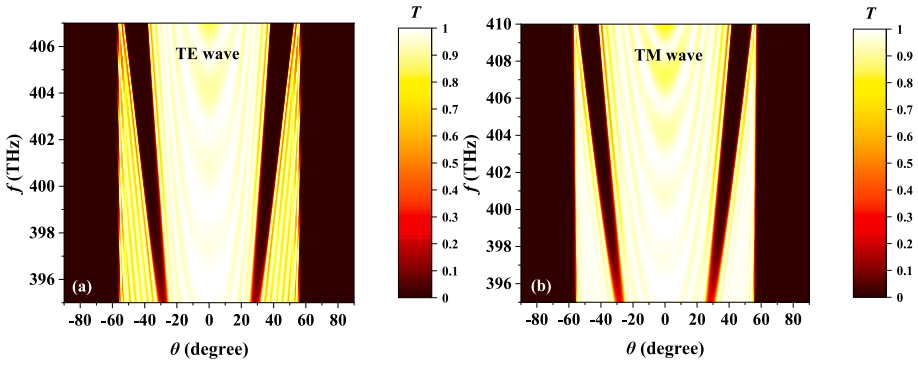

Fig. 10. The modulation of the three-channel ASWs by the adjustment of the incident frequency under (a) the TE wave and (b) the TM wave.

3.5. Four-channel ASWs under the cascade of MCPC1, MCPC2, and MCPC3

If the ENZ edge is combined with the DER1 and DER2, four-channel ASWs will be generated. In Fig. 13(a), for the TE wave, the four-channel phenomenon is maintained within the bandwidth of 398–404 THz. With the increase in frequency, the ranges of ASWs are reduced. If the incident frequency is 398 THz, the angle ranges are −55.2 ~ −38.2°, −27.2 ~

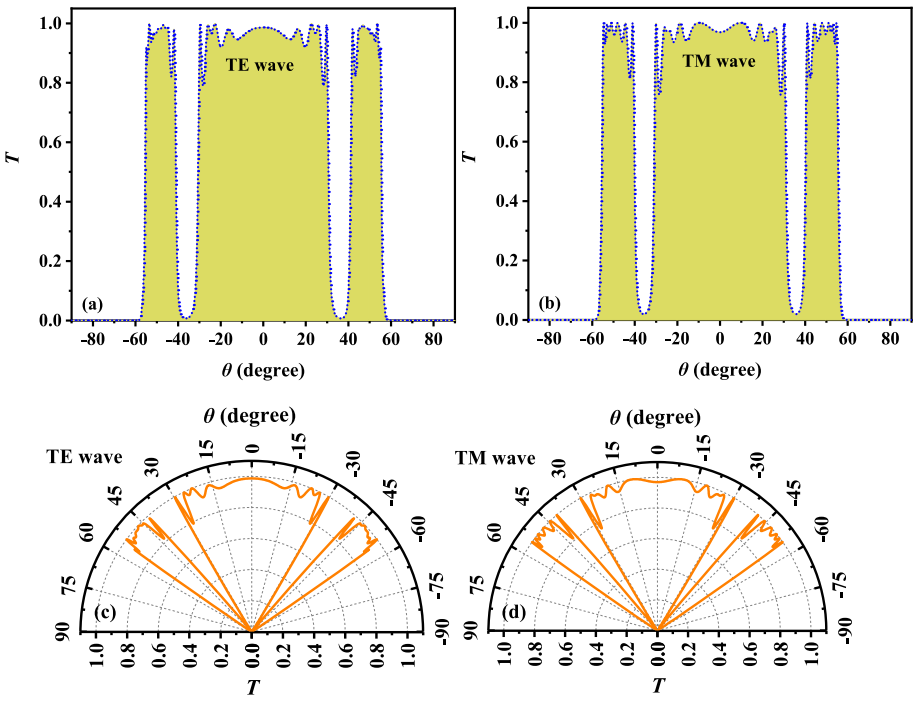

Fig. 11. The three-channel ASWs of 400 THz under the action of the ENZ edge and DER2 under (a) the TE wave and (b) the TM wave. Direction selection diagrams of (c) the TE wave incidence and (d) the TM wave incidence.

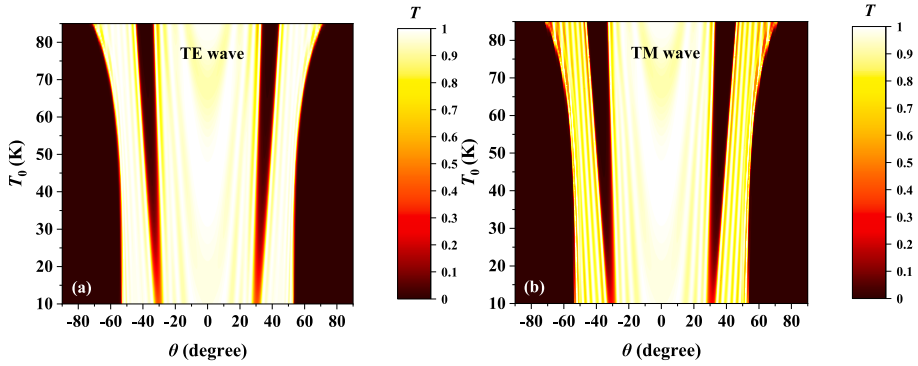

Fig. 12. The regulation of T_0 on the three-channel ASWs for (a) the TE wave and (b) the TM wave.

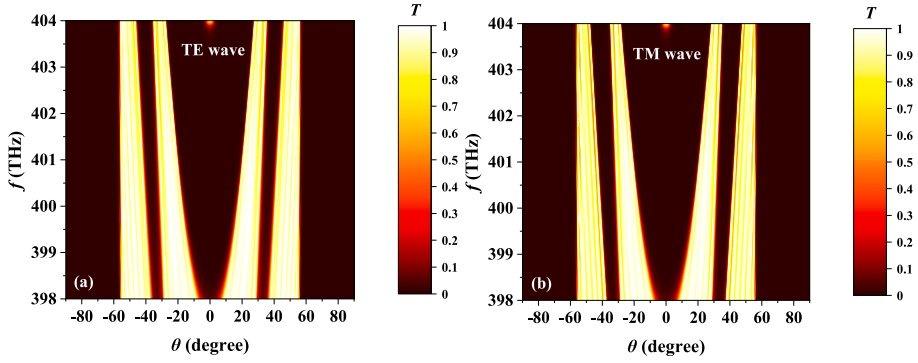

Fig. 13. The modulation of the four-channel ASWs by the adjustment of the incident frequency under (a) the TE wave and (b) the TM wave.

−9°, 9–27.2°, and 33.2–53.5°, and if the frequency becomes 404 THz, the corresponding values are −55.1 ~ −48.3°, −34.4 ~ −28.9°, 28.9–34.4°, and 48.3–55.1°. In Fig. 13(b), for the TM wave, the phenomenon of four-channel is also approximately maintained within the range of 398–404 THz. In the process of frequency drift, the maximum ranges covered by ASWs are −54.7 ~ −37.8°, −27.9 ~ −9.1°, 9.1–27.9°, and 37.8–54.7°, and the minimum ranges are −55.7 ~ −46.7°, −34.9 ~ −28.1°, 28.1–34.9°, and 46.7–55.7°. The maximum

ranges are obtained at 398 THz and the minimum ones are exhibited at 404 THz. Therefore, the increase in frequency also forces the reduction of the angle ranges.

In Fig. 14(a), four channels with a symmetrical arrangement are generated under the excitation of the TE wave with a frequency of 400 THz. The ranges of channels are −55 ~ −41.9°, −29.9 ~ −17.8°, 17.8–29.9°, and 41.9–55°. The overall transmittance is higher than 0.8, and the edge selectivity is obvious. In Fig. 14(b), supposing that the TM wave is incident, the ranges of the two channels are −55.2 ~ −40.9°, −30.3 ~ −17.7°, 17.7–30.3°, and 40.9–55.2°, which still presents a symmetrical arrangement, and the transmissivity and edge selectivity distribution are also maintained at a high level. The polar coordinates maps in Fig. 14(c) and (d) are also depicted to visually observe the edge selection characteristics of ASWs. Significantly, the four edges of the ASWs present excellent selectivity throughout the interval.

In Fig. 15(a), for the TE wave, when T_0 is 30 K, the regions covered by ASWs are −52.3 ~ −37.4°, −28 ~ −4.7°, 4.7–28°, and 37.4–68.9°, and when T_0 increases to 85 K, the corresponding angles are −70.3 ~ −46.6°, −32.2 ~ −26.5°, 26.5–32.2°, and 46.6–70.3°. In Fig. 15(b), under the case of the TM wave, the ASWs ranges at 30 K are −52.5 ~ −37.3°, −28.4 ~ −5.1°, 5.1–28.4°, and 37.3–52.5°, and the ASWs ranges at 85 K are −70.4 ~ −45.1°, −32.7 ~ −25.8°, 25.8–32.7°, and 45.1–70.4°. It can be observed that all the windows are skewed towards large angles, regardless of the polarization.

3.6. Error analysis and parameter influence

Considering that air layers are introduced into the single-channel ASWs, the thickness of the air layer may be affected in the etching process, so the influences of air layer thickness on ASWs are taken into account. According to the current technological level, the thickness errors of ±10% are discussed. In Fig. 16(a)–(d), no matter for the TE wave or the TM one, when the thickness error of the air layer is −10% or +10%, that is, when d_{Air} = 36 nm or 44 nm, the transmittance is always higher than 0.9 in the range of 220–1500 THz, and the angle selectivity is also very significant. It can be observed that the performance of ASWs will not be effectively affected even if the thickness of the air layer is inadvertently introduced into the error during the experiment.

In addition, due to processing issues, if the air layer is replaced with a low refractive index medium, SiO_2 can be considered, with a refractive index of 1.45. Compared with the air layer, SiO_2 has a higher refractive index, so the thickness needs to be reduced to 10 nm, and the other arrangement and medium of MCPC1 are unchanged. In Fig. 17(a), for the TE wave, ASW can also maintain high transmittance and angle selectivity in the low-frequency region below 480 THz. For the region above 480 THz, ASW is more seriously affected. The high transmittance range is compressed, and the smoothness of the edge is also reduced. In Fig. 17(b), the TM wave is less affected. In the region below 820 THz, ASW can still maintain a good level, while in the higher frequency region, the angle range and edge smoothness of ASW decrease slightly.

Considering that the periods of the host structure in MCPC2 are too large, which brings difficulties to the actual manufacturing, the influence of the periods is discussed here. For ease of representation, N is used to represent the number of periods. Since only two-channel ASW and four-channel ASW involve MCPC2, only these two cases are analyzed here. As can be seen from Fig. 18, the change of N has no obvious effect on the transmittance of the ASW, which is always higher than 0.85. The edge selectivity of the ASW will be reduced, which means that the rectangular feature of the ASW will be attenuated. As shown in Fig. 19, for both TE and TM waves, the transmittance of ASW gradually decreases with the increase of N and is eventually lower than 0.8. In addition, a drop in N also reduces the rectangular character of the window.

4. Conclusion

In this paper, the control of electromagnetic wave direction in space can be realized by cascading specific MCPCs structures. The edges of the ASWs depend on the ENZ edge of MCPC1 and DERs of MCPC2 and MCPC3, respectively. MCPC1 is used for the realization of single-channel ASWs, and the combination of MCPC1 and MCPC2 achieves the two-channel ASWs. The cascade of MCPC2 and MCPC3 induces three channels, and under the total action of MCPC1, MCPC2, and MCPC3, the four-channel ASWs will occur. A high degree of selectivity can be

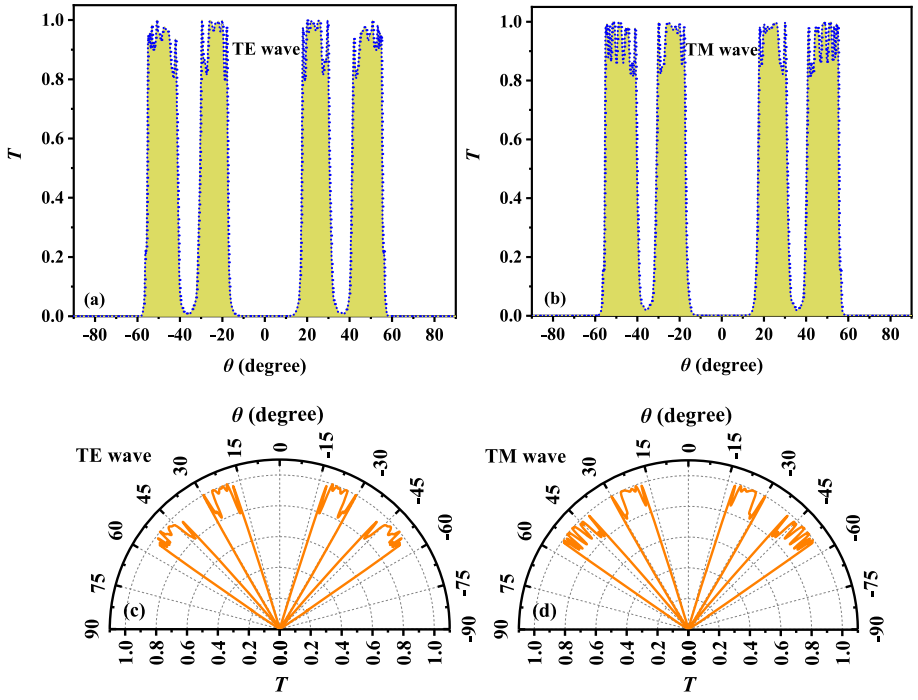

Fig. 14. The three-channel ASWs of 400 THz under the action of the ENZ edge, DER1 and DER2 under (a) the TE wave and (b) the TM wave. Direction selection diagrams of (c) the TE wave incidence and (d) the TM wave incidence.

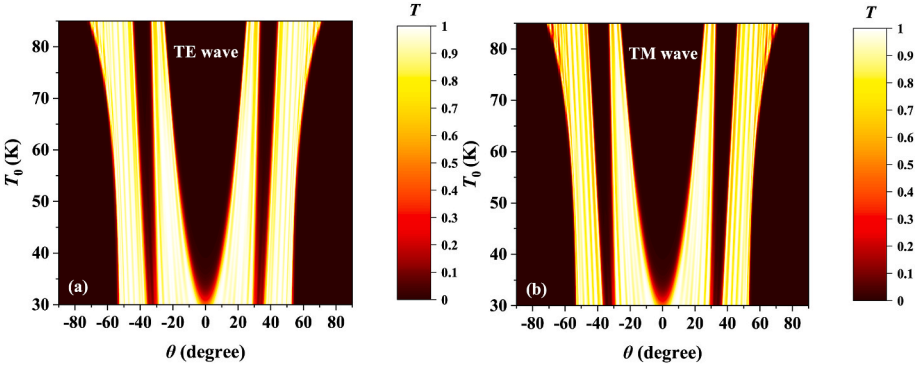

Fig. 15. The regulation of T_0 on the four-channel ASWs for (a) the TE wave and (b) the TM wave.

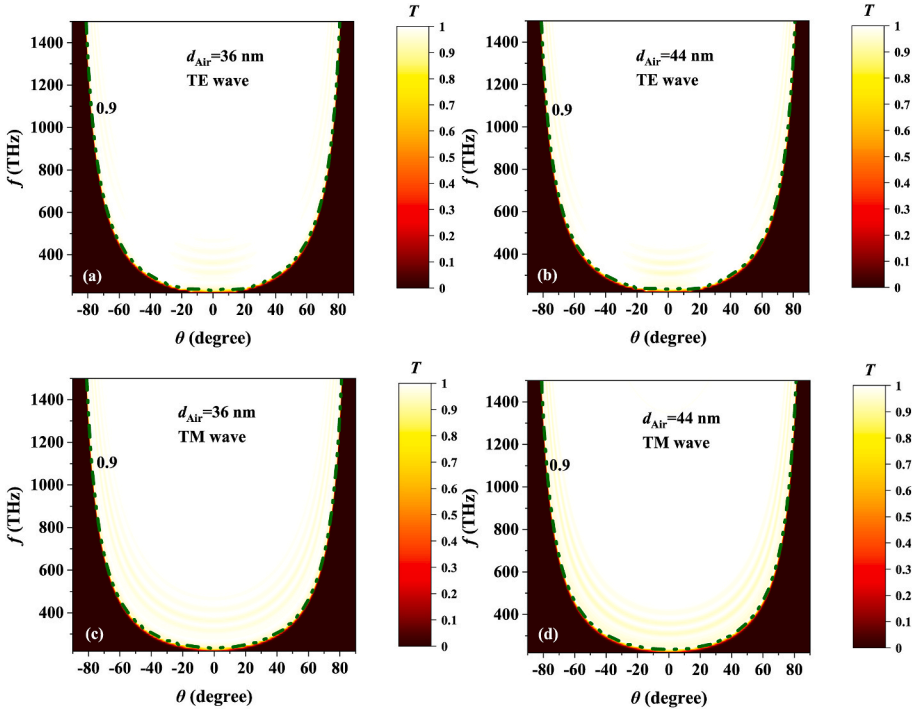

Fig. 16. Effects of air layer thickness error on the performance of single-channel ASWs, (a) $d_{Air} = 36$ nm, TE wave, (b) $d_{Air} = 44$ nm, TE wave, (c) $d_{Air} = 36$ nm, TM wave, (d) $d_{Air} = 44$ nm, TM wave. The double dotted lines in dark green are contours with a transmittance of 0.9.

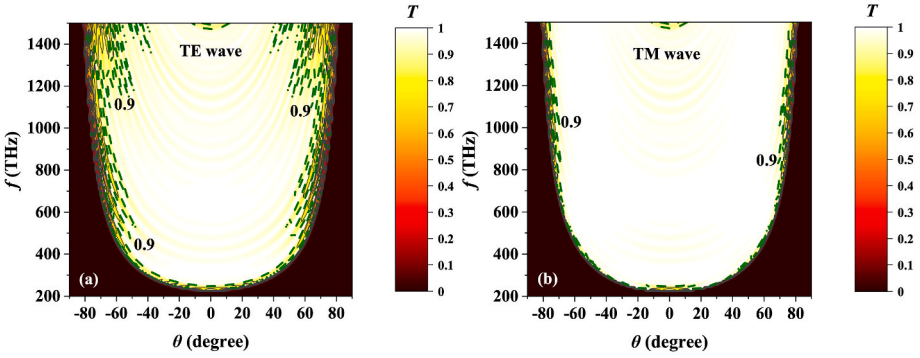

Fig. 17. When the air layer is replaced with the SiO_2 material with the thickness of 10 nm, the angle selection phenomenon of the ENZ edge is observed under the (a) TE wave and (b) TM wave.

achieved regardless of the angle transmission of several channels. Single-channel windows and dual-channel windows are pattern-free, and thanks to the ENZ characteristics of superconductors, the effective working bandwidth of single-channel windows spans 220–1500 THz. The three-channel and four-channel angle windows depend on polarization. The influences of temperature on ASWs are also significant. We

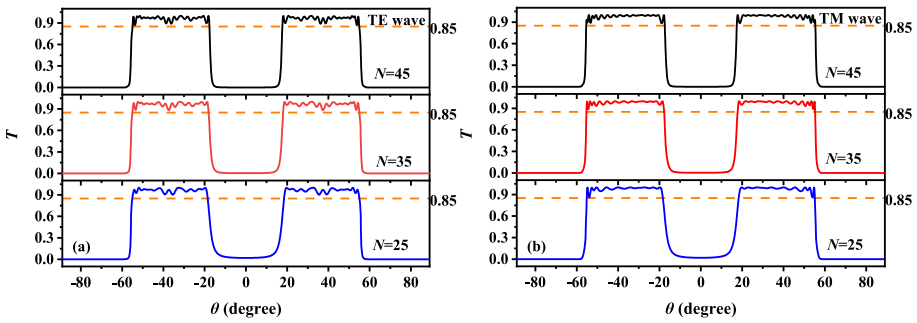

Fig. 18. Effects of period number N on double-channel angle window, (a) $N = 45$, (a) $N = 35$, (a) $N = 25$.

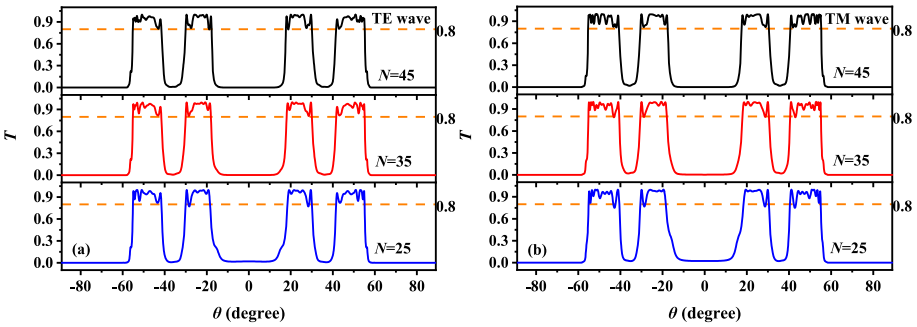

Fig. 19. Effects of period number N on four-channel angle window, (a) $N = 45$, (a) $N = 35$, (a) $N = 25$.

hope that the proposed multi-channel angular propagation structures can play a positive role in the field of antenna directional radiation, optical privacy protection, optical anti-counterfeiting, and so on.

CRediT authorship contribution statement

Bao-Fei Wan: Data curation, Formal analysis, Investigation. **Hai-Ning Ye:** Writing – original draft, Visualization. **Hai-Feng Zhang:** Conceptualization, Methodology, Supervision, Writing – review & editing.

Declaration of competing interest

The authors declare that they have no known competing financial interests or personal relationships that could have appeared to influence the work reported in this paper.

Acknowledgements

This work was supported by the Postgraduate Research & Practice Innovation Program of Jiangsu Province (Grant No. KYCX23_1004).

References

[1] K.Z. Yin, Y.R. Qu, S.E. Kooi, W. Li, J.X. Feng, J.A. Ratto, J.D. Joannopoulos, M. Soljačič, Y.C. Shen, Enabling manufacturable optical broadband angular-range selective films, ACS Nano 15 (2021) 19917–19923.
[2] H. Iizuka, N. Ngheta, E. Sugiura, Extremely small wavevector regime in a one-dimensional photonic crystal heterostructure for angular transmission filtering, Opt. Lett. 41 (16) (2016) 3829–3832.
[3] Y.C. Shen, C.W. Hsu, Y. Xiang Yeng, J.D. Joannopoulos, M. Soljačić, Broadband angular selectivity of light at the nanoscale: progress, applications, and outlook, Appl. Phys. Rev. 2 (2016), 011103.
[4] L. Grineviciutea, C. Babayigitb, D. Gailevičiusc, E. Borb, M. Turdueve, V. Purlysc, T. Tolenisa, H. Kurtb, K. Staliunas, Angular filtering by Bragg photonic microstructures fabricated by physical vapour deposition,", Appl. Surf. Sci. 481 (2019) 353–359.
[5] A. Alu, G.D. Aguanno, N. Mattiucci, M.J. Bloemer, Plasmonic Brewster angle: broadband extraordinary transmission through optical gratings, Phys. Rev. Lett. 106 (2011), 123902.
[6] Y. Shen, D. Ye, Z. Wang, W. Li, M. Soljacic, Metamaterial broadband angular selectivity, Phys. Rev. B 90 (2014), 125422.
[7] H. Huang, Z.X. Shen, Angle-selective surface based on uniaxial dielectric-magnetic slab, IEEE Antenn. Wirel. Pr. 19 (12) (2020) 2457–2461.
[8] Y. Gao, B.H. Li, R. Wang, Qi H. Yan, J.T. Huangfu, D.X. Ye, Polarization-independent broadband angular selectivity based on anisotropic diamagnetic metamaterial, IEEE Trans. Antenn. Propag. 70 (8) (2022) 7306–7310.
[9] E.D. Kosten, J.H. Atwater, J. Parsons, A. Polman, H.A. Atwater, Highly efficient GaAs solar cells by limiting light emission angle, Light Sci. Appl. 2 (1) (2013) e45.
[10] T. Komine, M. Nakagawa, Fundamental analysis for visible-light communication system using LED lights, IEEE Trans. Consum. Electron. 50 (1) (2004) 100–107.
[11] S.W. MacMaster, Privacy screen for a display, U.S. Patent 7 052 746 (2006).
[12] J. Guo, S. Chen, S. Jiang, Optical broadband angular filters based on staggered photonic structures, J. Mod. Opt. 65 (2017) 1–9.
[13] B.T. Schwartz, R. Piestun, Total external reflection from metamaterials with ultralow refractive index, JOSA B 20 (2003) 2448–2453.
[14] Q. Qian, C. Xu, C. Wang, All-dielectric polarization-independent optical angular filter, Sci. Rep. 7 (2017), 16574.
[15] B. Shi, Z.M. Jiang, X. Wang, Defective photonic crystals with greatly enhanced second-harmonic generation, Opt. Lett. 26 (15) (2001) 1194–1196.
[16] R.E. Hamam, I. Celanovic, M. Soljačič, Angular photonic band gap, Phys. Rev. A 83 (3) (2011), 035806.
[17] L.V. Alekseyev, E.E. Narimanov, T. Tumkur, H. Li, Yu A. Barnakov, M.A. Noginov, Uniaxial epsilon-near-zero metamaterial for angular filtering and polarization control, Appl. Phys. Lett. 97 (2010), 131107.
[18] P. Lodahl, A. Driel, I.S. Nikolaev, A. Irman, K. Overgaag, D. Vanmaekelbergh, W. L. Vos, Controlling the dynamics of spontaneous emission from quantum dots by photonic crystals, Nature 430 (7000) (2004) 654–657.
[19] H. Jiang, H. Chen, H. Li, Y. Zhang, S. Zhu, Omnidirectional gap and defect mode of one-dimensional photonic crystals containing negative-index materials, Appl. Phys. Lett. 83 (26) (2003) 5386–5388.
[20] Y. Chassagneux, R. Colombelli, W. Maineult, S. Barbieri, H.E. Beere, D.A. Ritchie, S.P. Khanna, E.H. Linfield, A.G. Davies, Electrically pumped photonic-crystal terahertz lasers controlled by boundary conditions, Nature 457 (7226) (2009) 174–178.
[21] B. Yang, Q. Guo, B. Tremain, R. Liu, L.E. Barr, Q. Yan, W. Gao, H. Liu, Y. Xiang, J. Chen, Ideal Weyl points and helicoid surface states in artificial photonic crystal structures, Science 359 (6379) (2018) 1221.
[22] R. Dalmisa, O.Y. Keskina, N.F. Ak Azema, I. Birlik, A new one-dimensional photonic crystal combination of TiO2/CuO for structural color applications, Ceram. Int. 45 (17) (2019) 21333–21340.
[23] C.R. Tubío, J.A. Nóvoab, Jorge Martín, F. Guitián, J.R. Salgueiro, A. Gil, Broadband terahertz ZnO photonic crystals fabricated by 3D printing, Ceram. Int. 45 (5) (2019) 6223–6227.
[24] Y.C. Shen, Optical broadband angular selectivity, Science 343 (2014) 1499–1501.
[25] H. Tanaka, I. Takai, H. Fujikawa, H. Iizuka, Nearly polarization-independent angular filters consisting of one-dimensional photonic crystals realized in the visible region, J. Lightwave Technol. 36 (2018) 2517–2523.

[26] Y.R. Qu, Y.C. Shen, K.Z. Yin, Y.Q. Yang, Q. Li, M. Qiu, M. Soljacic, Polarization-independent optical broadband angular selectivity, ACS Photonics 5 (2018) 4125.
[27] B.F. Wan, H.N. Ye, D. Zhang, H.F. Zhang, A variable refractive index sensor based on epsilon-near-zero spatial selection structure and its potential in biological detection, New J. Phys. 25 (2023), 023003.
[28] A.H. Alya, S.E.S. Abdel Ghany, B.M. Kamal, D. Vigneswaran, Theoretical studies of hybrid multifunctional $YaBa_2Cu_3O_7$ photonic crystals within visible and infra-red regions, Ceram. Int. 46 (2020) 365–369.